Journal of Quantitative Spectroscopy & Radiative Transfer 228 (2019) 27–46

Contents lists available at ScienceDirect

Journal of Quantitative Spectroscopy & Radiative Transfer

journal homepage: www.elsevier.com/locate/jqsrt

Internal electromagnetic waves, energy trapping, and energy release in simple time-domain simulations of single particle scattering.

R. Lee Panetta*, Siyao Zhai, Ping Yang

Department of Atmospheric Sciences, Texas A&M University, College Station, TX 77843, USA

ARTICLE INFO

Article history:
Received 16 July 2018
Revised 12 January 2019
Accepted 13 January 2019
Available online 27 January 2019

Keywords:
Single particle scattering
Internal electromagnetic waves
Femtosecond Gaussian pulses
Caustic evolution
Photonic nanojet

ABSTRACT

During the decay phase of the interaction of a femto-second Gaussian pulse with a single spherical particle, the presence of quasi-periodic short oscillatory bursts of electromagnetic energy at points in the near field outside the particle have been observed in three-dimensional simulations. Analogous behavior can be very easy produced and understood in simple one-dimensional scattering calculations. In two dimensions the situation immediately becomes more complicated and interesting. Here we discuss results from two-dimensional pseudo-spectral time-domain simulations of scattering from circular, elliptical, and hexagonal particles with the real index of refraction $m = 1.3$. Our focus is on how energy initially trapped within a particle after interaction with an incident Gaussian pulse is released over time, and we show two kinds of events that can result in "bursts" of energy release from the particles: (i) the coalescence of counter-propagating wave-packet-like electromagnetic field structures that have maximum amplitude near the surface of the particle, and (ii) encounters of individual packets with surface regions of high curvature. The coalescence events in the circular case show the dynamical origin of a two-dimensional form of "photonic nanojet." The two-dimensional simulations make clear the reason for quasi-periodic intermittent bursts at fixed near-field points outside the particle. Examination of field evolution shows that distinct near-surface internal field maxima, ostensibly the "source" of the emission bursts, are in fact inter-connected by caustic-like internal field structures that extend throughout the particle and have complex time evolution. The revealed intricacy of these connections suggests that understanding the origins of pulsed emissions in three dimensions, even for simple particle geometries, may be quite challenging.

1. Introduction

The subject of single particle scattering plays a fundamental role in developing methods to model the many interactions and feedbacks between atmospheric and oceanic particles (ice crystals, water droplets, soot, dust, wide varieties of aggregates, plankton, etc.) and the ambient electromagnetic radiation field. These methods find use both in direct models of atmospheric phenomena on time-scales ranging from seconds (weather simulations) to centuries (climate simulations), and indirect models of great utility in remote sensing of the atmosphere and oceans.

The work discussed in this paper had its origin in an attempt to understand how to economize on cpu time when using a particular method of studying single particle scattering that is based on a numerical simulation of a solution to Maxwell's equations. Commonly used methods can be divided broadly into two classes, "time-domain" and "frequency-domain" methods, depending on whether they are based on the equations themselves or a Fourier transform in time of the equations. Examples of the former are the Finite-Difference Time-Domain (FDTD: e.g. [1,2]) and Pseudo-Spectral Time-Domain (PSTD; e.g. [3,4]) methods, and an example of the latter is the Discrete Dipole Approximation (DDA; e.g. [5,6,7]). This short list could easily be made longer. The use that is typically made of the FDTD or PSTD is to simulate the electromagnetic interactions in and near a particle (the "near-field"), an effort that can involve considerable cpu time; the results of these calculations are recorded at points on or within some computationally convenient surface (a "Huygens surface") outside the particle, then mapped to large distances from the particle (the "far field") using some surface- or volume-integral based method called a "near-to-far-field" transformation. In the DDA method, the far-field is the sum of the contributions of individual dipoles. The FDTD and DDA are exact numerical methods, as is the T-matrix method [8–10].

The near-to-far field mapping (see, e.g. [11] for a discussion) commonly is done frequency-by-frequency, and a determination

* Corresponding author.
E-mail address: panetta@tamu.edu (R.L. Panetta).

https://doi.org/10.1016/j.jqsrt.2019.01.015
0022-4073/

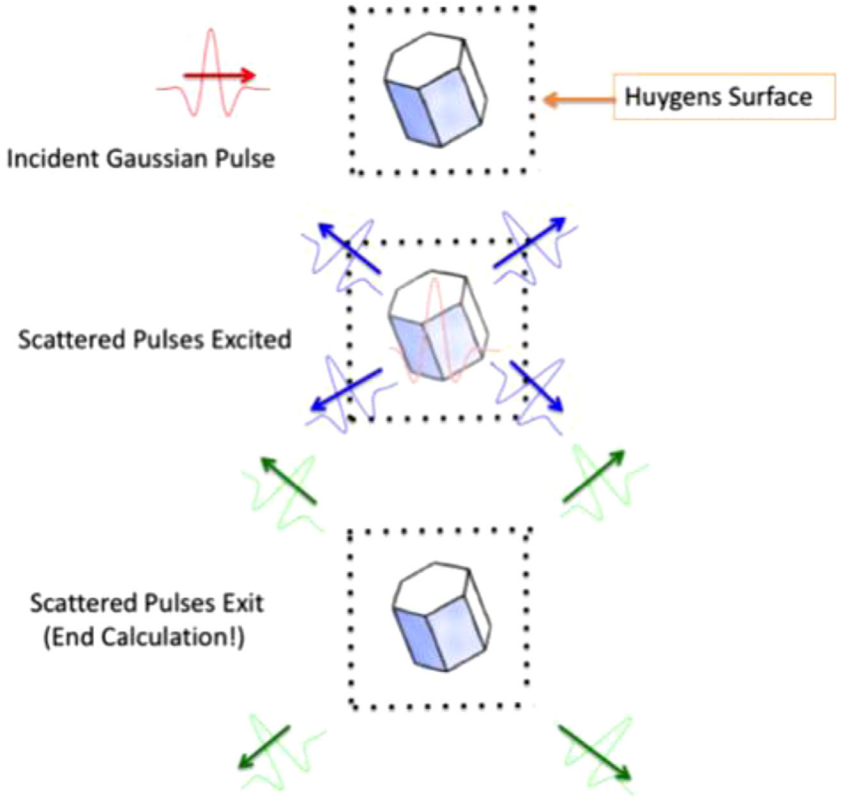

Fig. 1. Simple conception of pulse interaction.

must be made of when to stop the integration in the time-domain simulation of the near field evolution. This is a particularly important consideration when particles having a size large compared to the wavelength(s) incident on the particle are under study. The cpu time rises rapidly as the relative particle size, and with it the relative computational domain size, increases. The non-dimensional measure of the relative particle size we use is the size parameter x, defined in terms of a characteristic linear dimension a (e.g. the radius of a spherical particle, or the radius of a circumscribing sphere for a non-spherical particle) and a characteristic wavelength λ or wavenumber k by

$$x = \frac{2\pi a}{\lambda} = ka \tag{1.1}$$

Given current computational technology, in-depth study of scattering properties over an interesting range of particle shapes, compositions, and indices of refraction is limited to size parameters roughly in the range of 150–200. We were using the PSTD in this range, and were interested in finding a way to determine a priori when to stop our numerical time integrations of the near field before passing the results to the near-to-far-field calculation.

The particular kind of calculation we were doing involved an incident Gaussian pulse of electromagnetic radiation. In concept, the idea was simple (see Fig. 1): an incoming pulse would interact with an isolated particle over a period of time, with "eventual" radiation of the incident energy, and the calculation could be stopped once the particle was sufficiently emptied of the energy, in the sense that further integration would have no appreciable effect on the temporal Fourier transforms needed for the near-to-far-field transformation.

Ignored in this simple view is the definite possibility that some energy could remain "trapped" in the particle for a time, and that the manner in which the energy "eventually" is released might depend on particle geometry (not to mention particle composition) could be itself both interesting and important to the design of time-domain computations. One advantage, in fact, of using a time-domain method is the immediate view it can provide of the evolution of coherent field structures that may only leave a shadow of their nature in frequency domain simulations, a shadow whose physical origin might be more difficult to understand.

In a preliminary attempt to understand the rate and nature of the radiation of energy from a simple homogeneous spherical particle which had undergone an interaction with an incident Gaussian pulse, data were gathered from a three-dimensional PSTD calculation at points outside the particle, points situated at centers of faces of a cube outside the particle (See Fig. 2a). Time series of the vertical component of the electric field that resulted in two PSTD calculations using homogeneous spherical particles are shown, for $x = 30$ and $x = 80$, in Fig. 2b and c.

While it was clear that amplitudes at all points showed an overall decay with time, an unexpected feature of the time series was the presence of intermittent bursts of amplitude in the process of this decay. The existence of bursts in themselves suggested a difficulty in determining when to stop a calculation based on instantaneous values of field strength. More intriguing was the evidence that the bursts seemed, especially in the case of the smaller particle, to have a characteristic structure and to occur at something like regular intervals. The bursts seemed to indicate some interesting events in the evolution of the electromagnetic field in the particle after the "main" signal of the incident pulse had passed by the particle.

A little thought suggested how similar intermittency at points outside the particle could arise in the case of an incident Gaussian pulse in simple one-dimensional model, in which a "particle" was simulated by a permittivity pattern that was constant at a value above 1 in a localized region. In physical terms, this would be a model of a pulse normally incident on an infinite homogeneous slab, the slab itself oriented normal to the x axis in a Cartesian

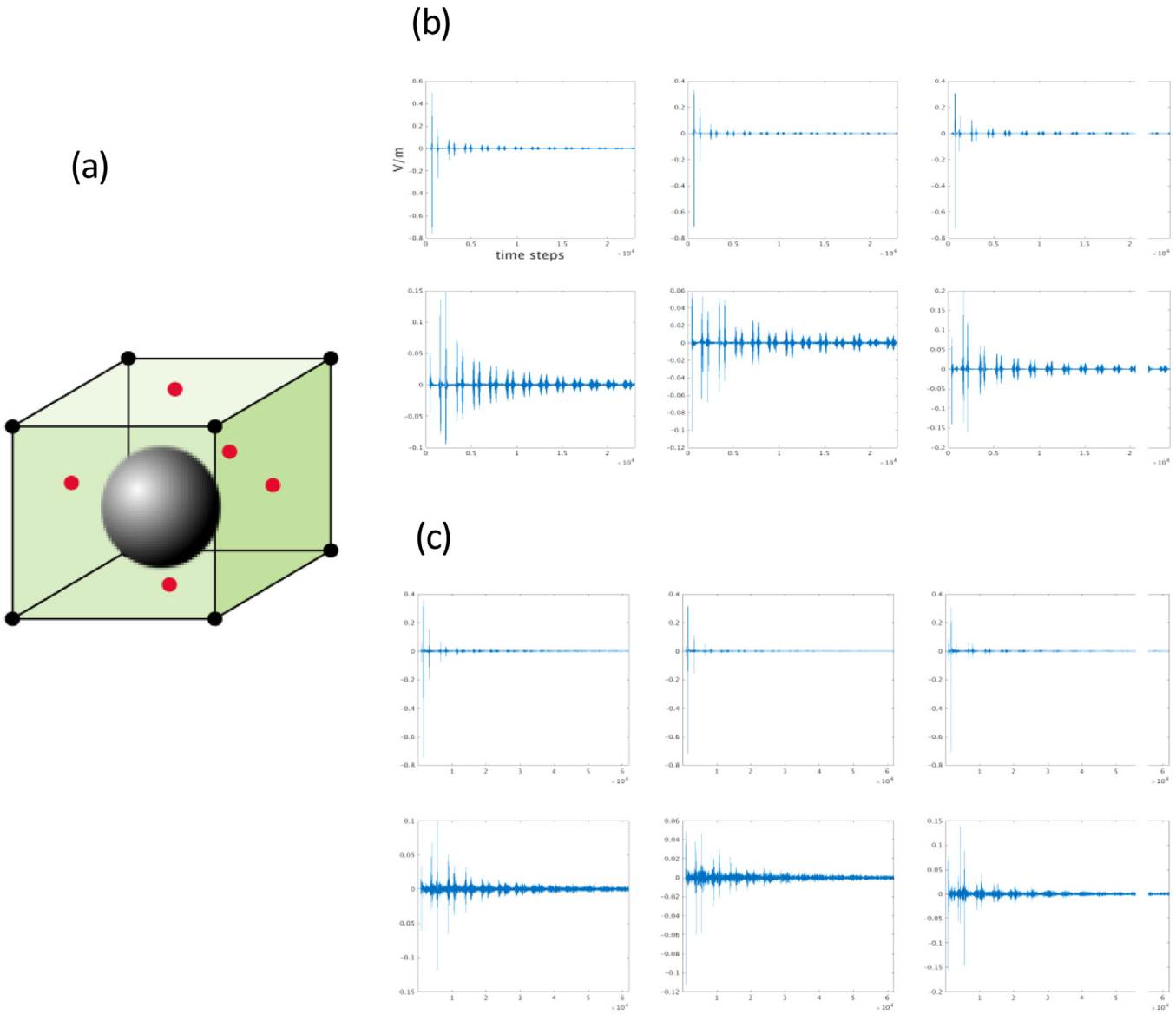

Fig. 2. Time dependence of the electromagnetic field component E_z at the six points centered on faces of Huygens surface indicated in (a) for spherical particles with size parameters (b) $x = 30$ and (c) and $x = 80$.

coordinate system. With electromagnetic fields

$$\boldsymbol{E} = E_y \hat{\boldsymbol{y}}$$
$$\boldsymbol{H} = H_z \hat{\boldsymbol{z}} \tag{1.2}$$

Maxwell's equations have the simple form

$$\frac{\epsilon}{c}\frac{\partial E_y}{\partial t} = -\frac{\partial H_z}{\partial x}$$
$$\frac{1}{c}\frac{\partial H_z}{\partial t} = -\frac{\partial E_y}{\partial x} \tag{1.3}$$

and the presence of a "particle" can be modeled by a localized departure of the permittivity from unity in a region between $x = x_1$ and $x = x_2$:

$$\epsilon(x) = \begin{cases} 1 & x < x_1 \\ \epsilon_p & x_1 \le x \le x_2 \\ 1 & x > x_2 \end{cases} \tag{1.4}$$

Fig. 3a displays some results from a PSTD simulation (with a 1-d version of the UPML) of a solution to Eqs. (1.3) and (1.4)) in the case of a Gaussian pulse with center wavelength 0.55 μ incident on such a particle with index of refraction $m = 1.3$. What is illustrated in the figure is the electric field component $E_z(t,x)$: in the figure time (on the horizontal axis) is scaled by the time it would take the pulse to cross the particle. The simple events of refraction and reflection are clear, and it is easy to understand how "pulses" appearing at fixed points outside the particle would occur. In fact, as Fig. 3a and b indicate, the amplitudes of the pulses are well predicted by arguments based on Fresnel's Laws (indicated on the figure by dotted lines denoted "Fresnel predictions" for successive events).

The next logical step was to consider a two-dimensional problem, one known on the basis of ray-tracing studies to have more interesting phenomenology, and on the basis of frequency domain studies to have complicated geometric structure [12,13]. The PSTD time-integrations we made clearly showed the presence of wave fields traveling within the particle, and totally different mechanisms for generating "pulses" of departing radiation than 1-d calculations could show. In this paper we focus on two particularly simple ways pulses are generated, leaving for later a more detailed examination of how the two are modified by changes

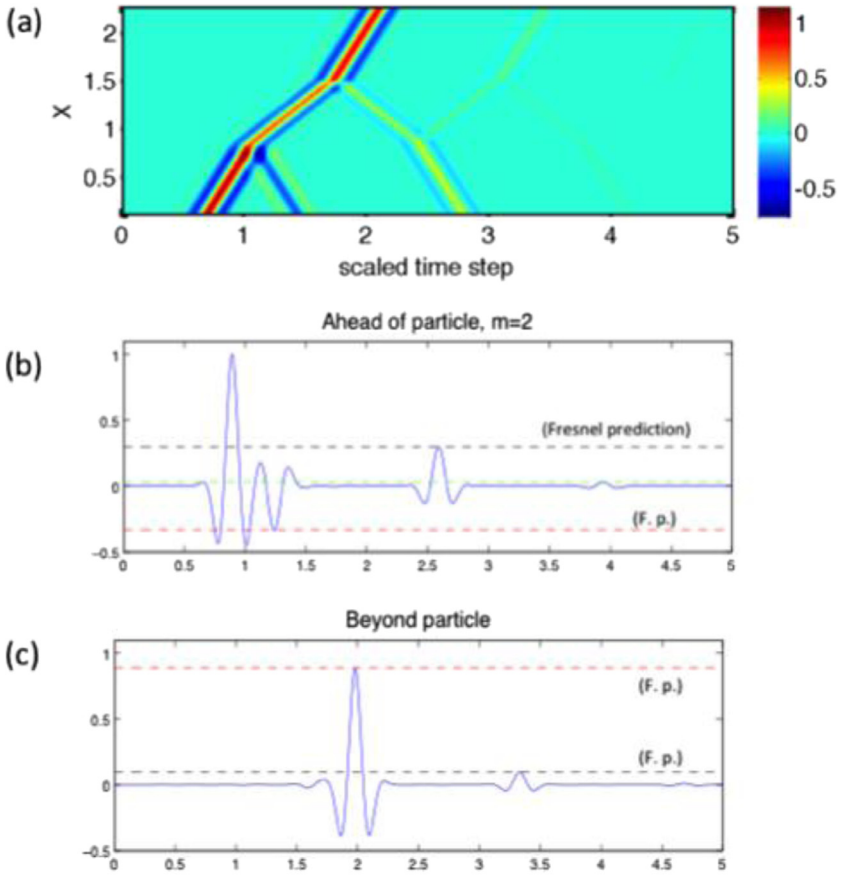

Fig. 3. One-dimensional calculation: PSTD-computed electric field as function of position and time (a); PSTD-computed electric field amplitudes as function of time at two fixed positions, one ahead of particle (b) and the other beyond particle (c). Dotted lines in (b) and (c) indicate Fresnel predictions.

in geometry, index of refraction, angle of incidence, or incident pulse shape. Accordingly, we consider just one central wavelength, 0.55 μ, for the incident Gaussian pulse, a single index of refraction for $m = 1.3$ (ice) and unit magnetic permeability for the particles, and normal incidence. The e-folding time for the pulse at a fixed point was chosen to be 1.7×10^{-15} sec for most of the results, though in a few cases discussed below the sensitivity of pulse duration to doubling or halving was tested.

The two-dimensional problem that we pose can be thought of as the case of a cylindrical particle (of specified cross-section) illuminated by an incident wave or wave packet approaching at an angle normal to the cylinder axis. We will study the TE case, in which the incident field is polarized parallel to the cylinder axis, and use the model equations

$$\frac{\epsilon}{c}\frac{\partial \boldsymbol{E}}{\partial t} = \nabla \times \boldsymbol{H}$$
$$\frac{1}{c}\frac{\partial \boldsymbol{H}}{\partial t} = -\nabla \times \boldsymbol{E} \qquad (1.5)$$

with

$$\boldsymbol{E} = E_z\hat{\boldsymbol{z}},\ \ \boldsymbol{H} = H_x\hat{\boldsymbol{x}} + H_y\hat{\boldsymbol{y}} \qquad (1.6)$$

The presence of a particle is recorded by the spatial dependence of the permittivity, $\varepsilon = \varepsilon(x, y)$, and in this study we considered cases of circular, elliptical, and hexagonal departures from $\varepsilon = 1$.

All of the PSTD calculations were conducted in a computational domain bounded by a uniaxial perfectly matched layer (UPML); some details can be found in [11]. As mentioned above, the central wavelength in the Gaussian pulse will be held at 0.55 μ and the index of refraction at $m = 1.3$. A shaped pulse necessarily includes wavelengths other than the central one; the PSTD method we use assumes the same index for all the component wave

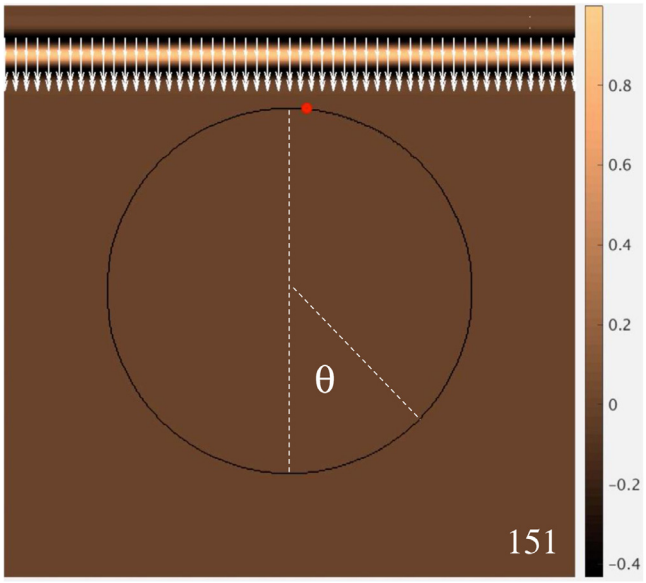

Fig. 4. The instantaneous E_z field at timestep 151. The red dot indicates one of two $|E_z|$ maxima within the particle: its angular position at this time is $\theta \approx 176^o$. The other maximum is at a position symmetrical about the particle centerline and is not indicated. The image is from timestep 151, where the time step increment is $\delta t \sim 2.62 \times 10^{-17}$ s. (For interpretation of the references to color in this figure legend, the reader is referred to the web version of this article.)

numbers and our simulations are consequently "non-diffusive" ones. (See [14] for a demonstration of the relatively modest differences between diffusive and non-diffusive calculations in the case of a spherical raindrop.)

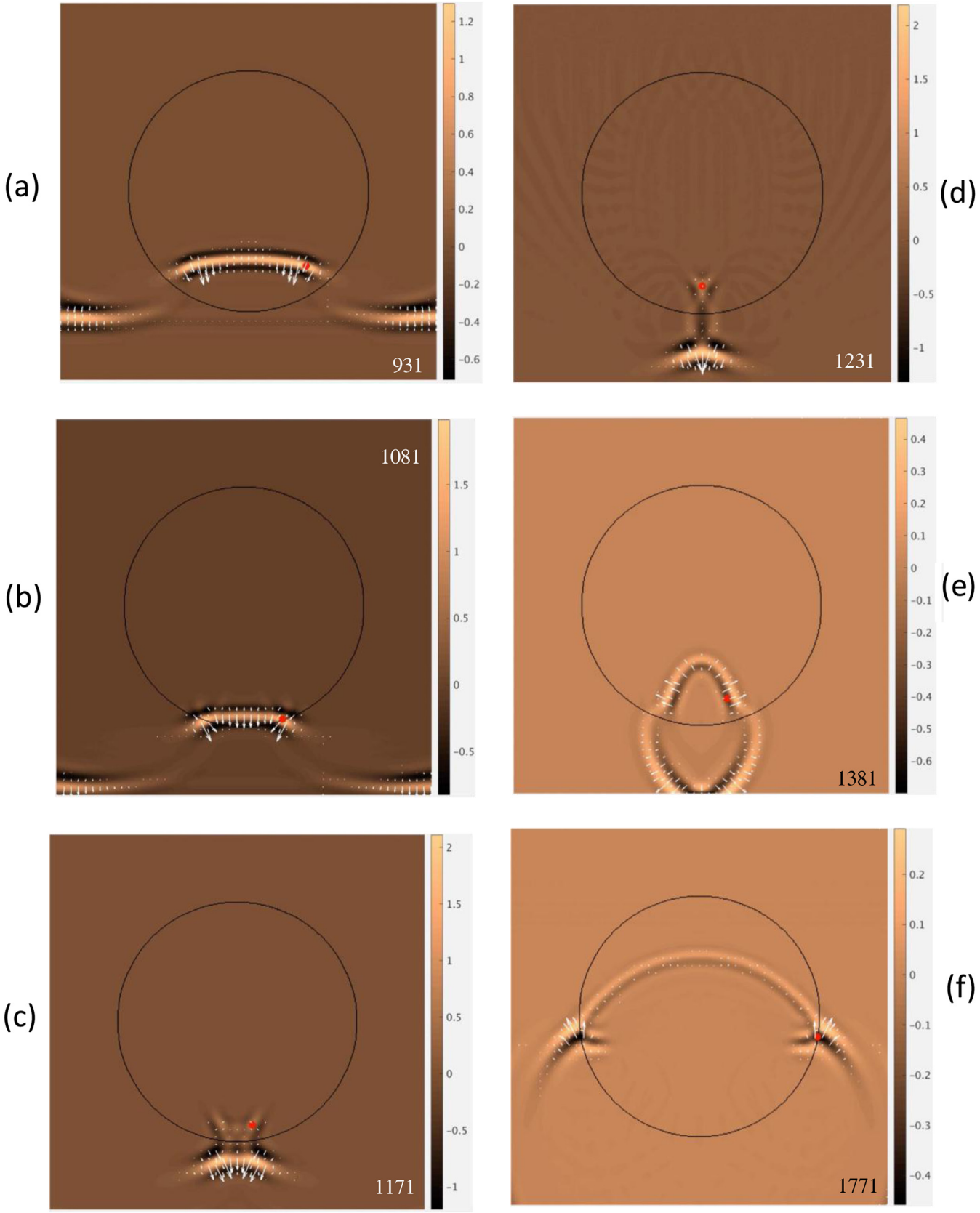

Fig. 5. (a–f) Incident Gaussian pulse interacting with cylindrical crystal with circular cross-section: timesteps 931, 1081, 1171, 1231, 1381, and 1771. (g–l). Continuation of previous figure: timesteps 2371, 2461, 3601, 3751, 4861, and 5041 (m). The Ez field at timestep 2101, which is intermediate between the times of f and g.

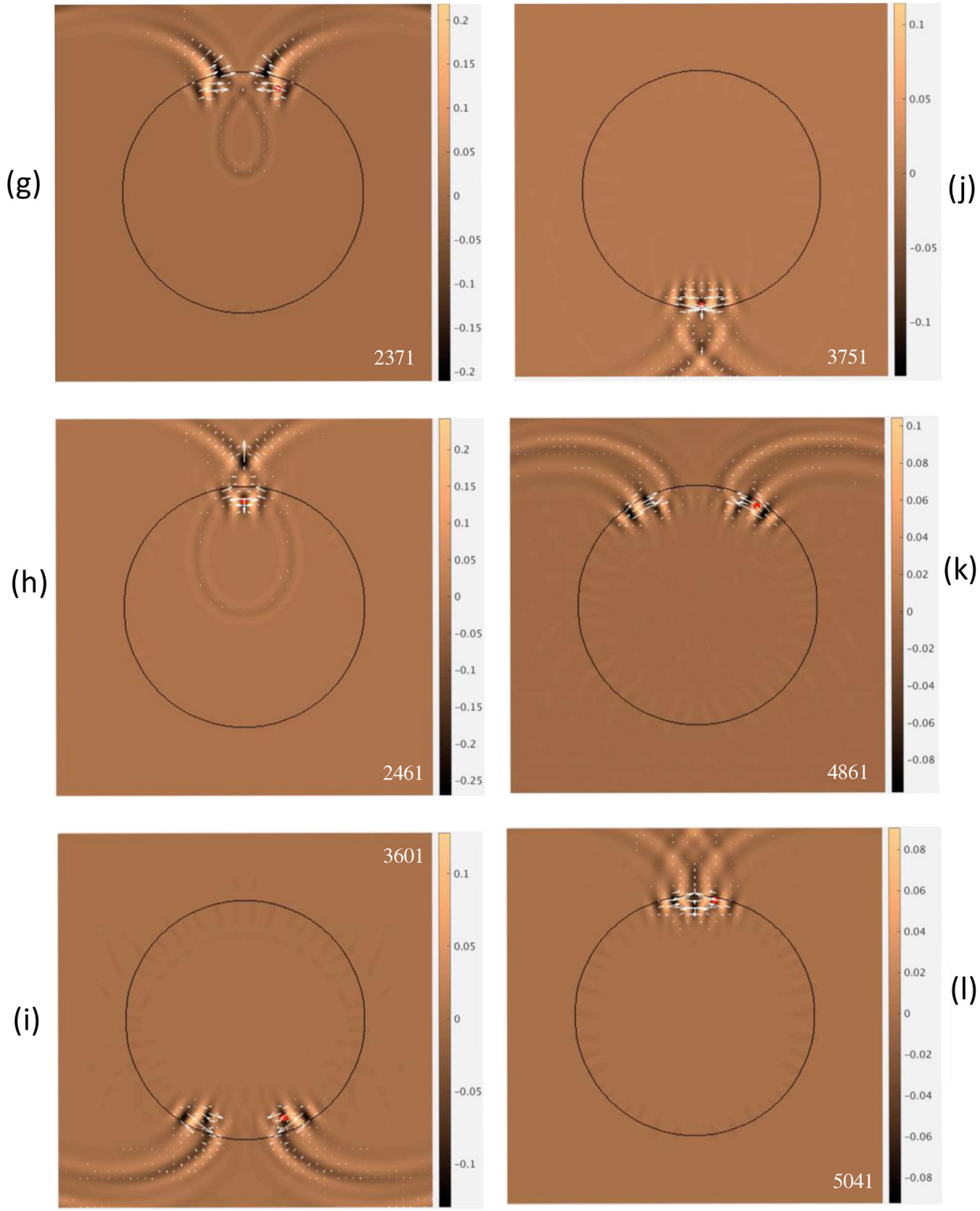

Fig. 5. Continued

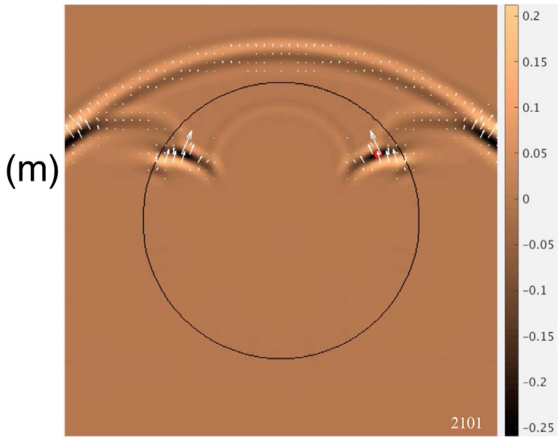

Fig. 5. Continued

Section 2 of this paper examines the case of an infinite cylinder of circular cross section, and introduces a first mechanism of pulse generation, a consequence of a particular evolution of the internal wave field. The wave fields at times show features of "traveling waves" with maximal amplitude near the surface, apparently traveling at a speed intermediate between the speed in air and in ice. In Section 3 we review a very simple model of how a traveling wave solution to Maxwell's equation could exist and how the speed of travel is determined. In Section 4 we return to two-dimensional calculations of particles with two different cross-sections, namely elliptical and hexagonal, and demonstrate another way pulses are generated. Section 5 contains a brief summary discussion.

2. Circular cross section: pulses from interactions of "counter-propagating waves."

Figs. (4 and 5a–f, g–l) show instantaneous fields of $E_z(x,y,t)$ for a particle with circular cross section and $x = 30$. In each panel, the white arrows indicate the local Poynting vector

$$\boldsymbol{P} = \boldsymbol{E} \times \boldsymbol{H},$$

which indicates the local flux of electromagnetic energy, and which in our case is necessarily horizontal. Times recorded in these and following figures are in terms of multiples of computational timestep $\delta t \sim 2.62 \times 10^{-17}$ sec. Fig. 4 shows the incoming pulse beginning to interact with the particle, and has two other features indicated that will be useful in subsequent discussion. The red dot, slightly to the right of the center line, indicates a point of maximum amplitude of the E_z field *within* the particle. The maximum is slightly off center because the internal field is already reacting to the leading edge of the pulse but at an amplitude too small to be visible in the color scheme of the figure. The angular position of this maximum, with the angle determined counterclockwise from the forward-scattering direction as indicated in Fig. 4, was recorded at each timestep for diagnostic calculations that are discussed below. Because of the symmetry of the problem, there is another maximum on the other side of the particle near $-178°$. This is not shown here or in subsequent figures relating to the circular particle, nor is it shown later in figures for cases particles considered with the same symmetry with respect to pulse propagation direction.

Fig. 5a and b show that the part of the incoming pulse that is outside the particle has progressed farther than the part that has encountered the particle, as would be expected from the differences in indices of refraction. The figures also show that the internal energy flux appears to be focused toward the forward scattering direction, and that the maximum amplitude of the electric field is near the surface of the particle.

Fig. 5c shows a time just after the two maxima have coalesced, moved further inward, then started to "split" symmetrically apart. In animations of the field evolution, this coalescence and "splitting" has the appearance of two counter-propagating wave packets with maximum amplitude near the surface passing through each other. The maximum amplitude in the entire field is at this time concentrated in a relatively narrow pulse moving off in the forward-scattering direction, perhaps a version in this computation of a "photonic nanojet" [15]. After this stage, the evolution of structure in the field may be loosely described as dominated by a time-evolving mixture of wave-packets with maximum amplitude near the surface of the particle, and internal curvilinear concentrations or beams of amplitude representing caustic-like features. Although at times the packets may appear to be highly localized near the surface, they have no clear relation to what are classically called "electromagnetic surface waves [16,17,18].

The Fig. (5e–l) suggest that the electromagnetic energy leaves the particle only slowly (more on this below) from the particle as the counter-propagating near surface maxima make their way around the particle until they meet and coalesce, at which times bursts of energy are shed alternately in the direct forward- and the direct back-scattering directions. Fig. 5m, corresponding to a time between those of Fig. 5f and g, illustrates features of electric field structure upon which we will comment below. In viewing the images, it should be kept in mind that while the color scheme changes only a little, the figures are constantly being rescaled to keep field structure clearly discernible: in fact the true amplitude is decreasing with time. This rescaling can be seen by the values indicated by the color bar included in each panel. (The time evolution of internal energy will be shown more clearly in Figs. 6–8 below.)

The major releases of energy that occur in bursts in the forward and backward directions give an interesting interpretation to the familiar forward and backward peaks in the phase function. The panels in Fig. 5 furthermore make it clear that at fixed points outside the particle, there should be intermittent bursts of oscillatory E_z as the curvilinear wave-fronts outside the particle (cf. Fig. 5i and k) that are connected to the near-surface wave packets sweep by the points. Time series at individual points (not shown) would show behavior qualitatively similar to that seen in the case of 3-d simulations (Fig. 2b and c).

Turning to a consideration of the overall evolution of electromagnetic energy with time, we first represent this evolution in a manner motivated by [14]. Fig. 6 shows evolution of field energy in two different ways. Fig. 6a shows the energy at a fixed distance

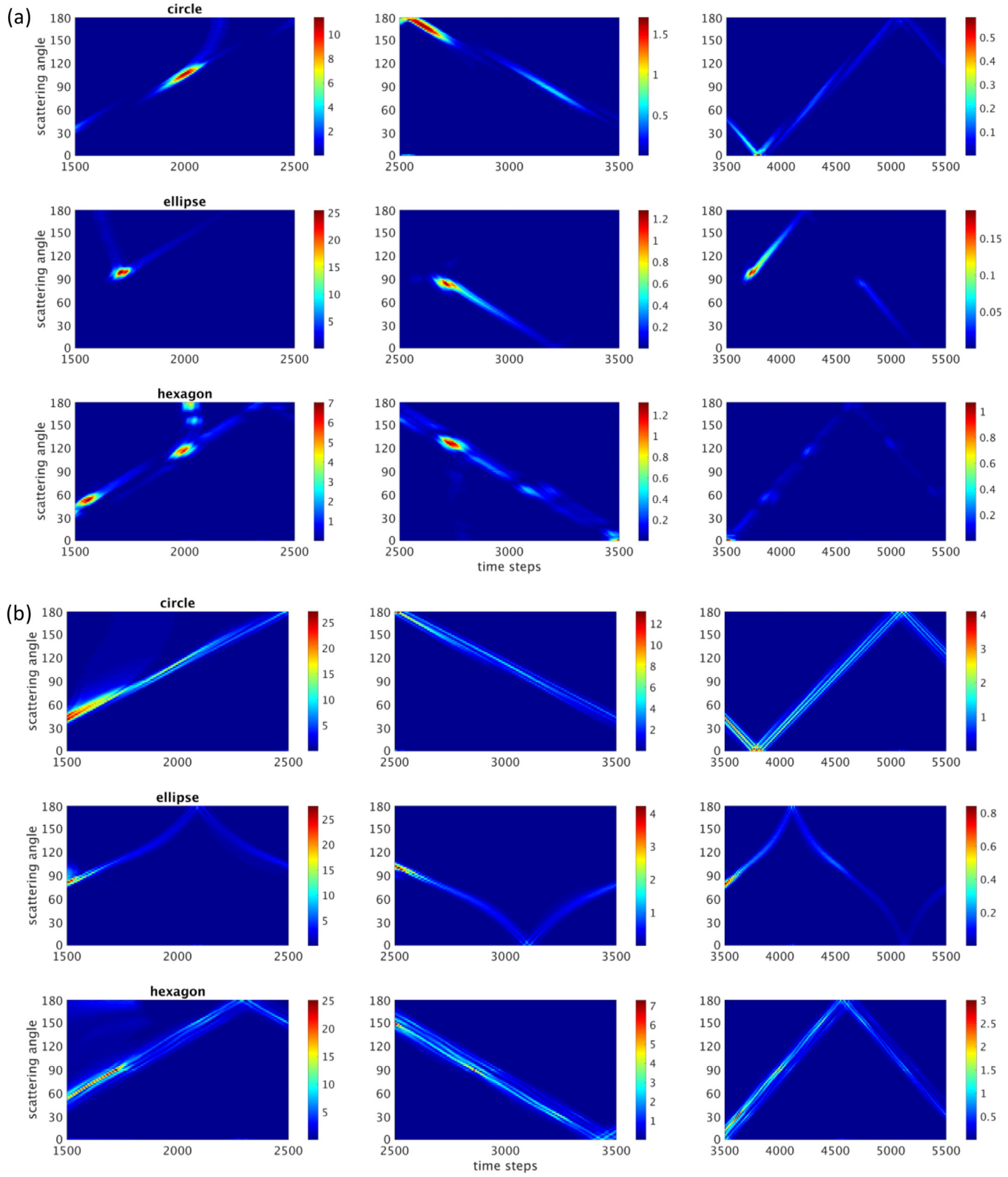

Fig. 6. Energy angle-time diagrams for circle, ellipse, and hexagon: (a) at a fixed distance outside the particle and (b) total inside the particle. Panels in the same row are for successive intervals of time. See text for details.

outside the particle (but not in the absorbing boundary layer), as a function of the angle θ (defined in Fig. 4) and time. The part of the evolution shown is after timestep 1500, which is after the main part of the incident pulse, as well as the first forward-scattering pulse, has passed out of the computational domain; it is between the times of Fig. 5e and f. Using the symmetry of the simulation we need only record the θ range [0, 180]. Fig. 6b shows the total energy within the particle, again as a function of angle and time, but recorded not in terms of energy at a fixed position, but instead in terms of the energy in a cone of width 2° centered on the

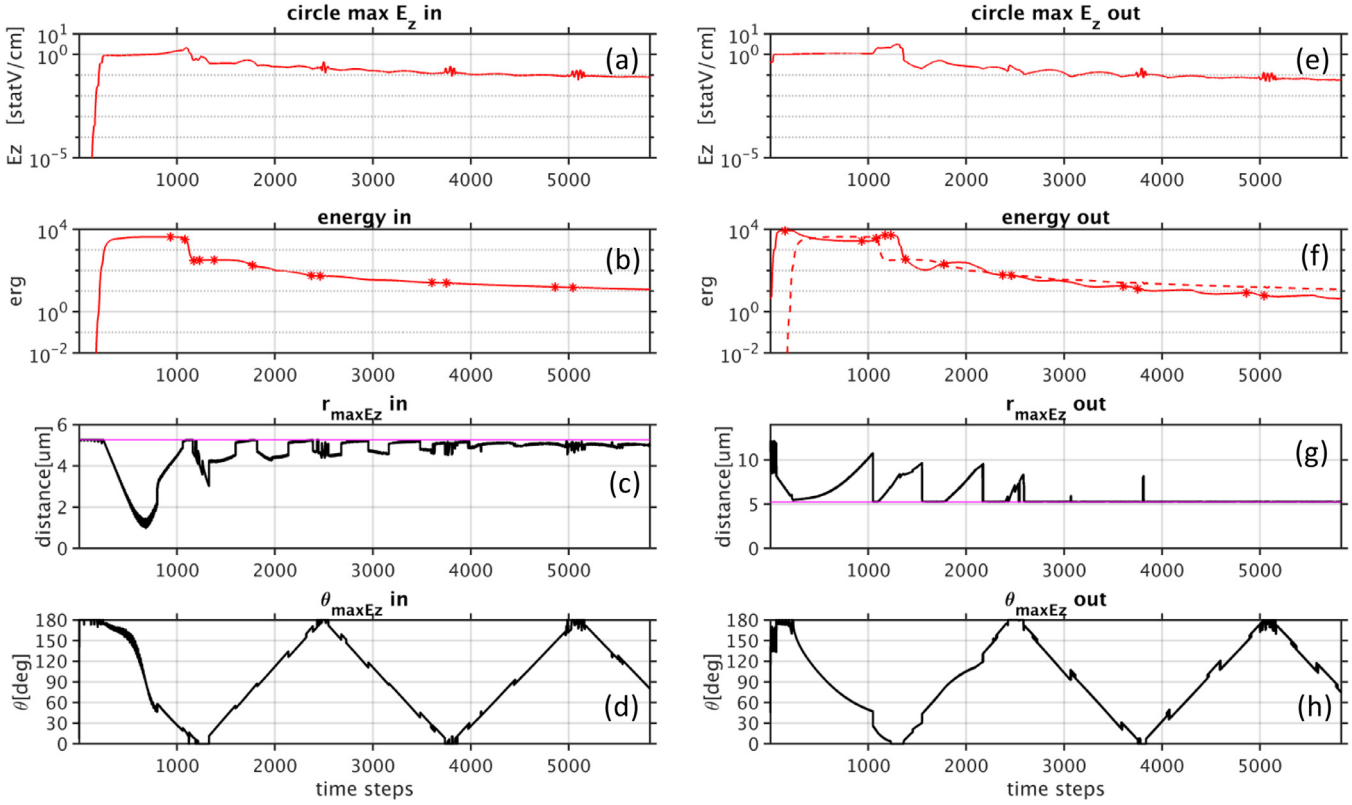

Fig. 7. Time series of data gathered inside (a–d) and outside (e–h) the circular cross-section particle. Asterisks in the panels in the second row indicate times of Fig. 4a–l. Shown are: pointwise maximum of $|E_z|$ (a and e); total electromagnetic energy (b and f); distance of pointwise maximum from particle center (c and g), with red line indicating particle boundary; and angle at which pointwise maximum occurs (d and h), with forward direction = 0°. See text for more details. (For interpretation of the references to color in this figure legend, the reader is referred to the web version of this article.)

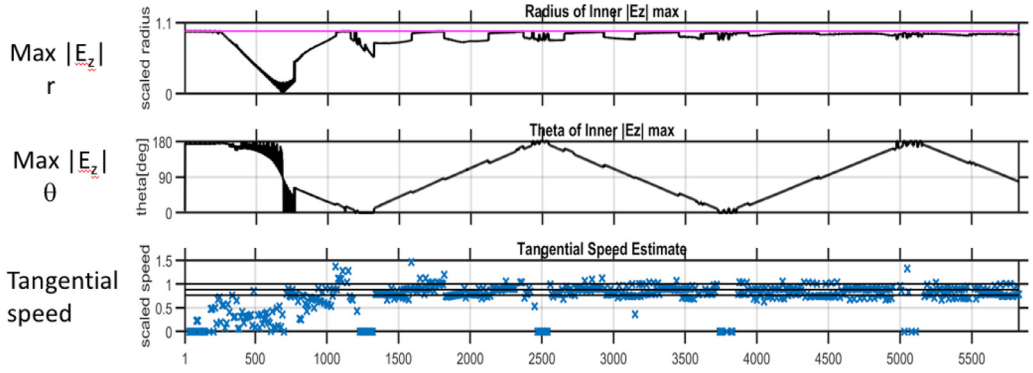

Fig. 8. Tangential speed estimates for movement of $|E_z|$ maxima constructed from data shown in Fig. 5. The speeds are normalized by the speed of light c; see details in the text.

angle θ. The upper row of three panels in 6a and 6b are for the circular case; lower rows are for the elliptical and hexagonal cases discussed later. The rows are split into three successive time intervals in order to handle the decay of energy with time: successive panels in a row use re-allocation of colors to energy levels (note the colorbar values), this assignment being held constant during the time interval of each panel.

Because the simulation is conducted in the near field, not all features of the data gathered outside the particle are easy to interpret in terms of implications for the far field. The amplitude maxima occurring at near backscatter in the second panel for the circle in Fig. 6a, and the one at the forward scattering angle in the third panel are as would be expected (cf. Fig. 5g and j). But the maximum at about $\theta = 105°$ near timestep 2000 in the first panel is a little harder to interpret. It also shows up in the internal energy plot at about the same time. Examination of the entire field at these times shows that the energy being "launched" at about timestep 1771 (Fig. 5f) reaches the sampling radius during the interval of the amplitude maximum in the first panel.

The second two panels in Fig. 6a and especially in Fig. 6b indicate, aside from the decay of internal energy, that there is an approximately constant angular velocity associated with the movement of energy. To look more closely at this movement, we consider another method of analysis that also is useful for showing the relation between the release of energy from the particle and features of the wave field, a way that will prove particularly useful when we consider other particle shapes below. Recall that the red dots in Fig. 5 panels indicate the location of maximum $|E_z|$ inside the particle. Values for these amplitudes and corresponding positions, along with values of total internal electromagnetic energy

inside and outside the particle, were recorded during the simulations and are displayed in Fig. 7.

The figure shows features of the electromagnetic field inside (left-hand column) and outside (right-hand column) the particle. Here "outside the particle" means in the part of the computational domain outside the particle but exclusive of the UPML. (The presence of this layer means that all field quantities should eventually decay with time.) Panels (a) and (b) show, respectively, a time series of the value of maximum $|E_z|$ at any interior grid point and the total electromagnetic energy (both electric and magnetic) within the particle. The asterisks on the curve in the internal energy time series (7b) indicate the times of the images shown in Fig. 5; the asterisks on the series for external energy (7f) have the same meaning. The interior grid point maximum $|E_z|$ (7a) at first rises as a part of the incident pulse begins to influence the field within the particle, remains relatively constant until the "focusing" of energy seen in Fig. 5b and c cause a local rise at the region from which the first forward pulse will be emitted, and then drops as that pulse is emitted. At this time total internal electromagnetic energy drops sharply, while both the maximum grid point $|E_z|$ outside the particle and total outside electromagnetic energy (Fig. 7e and f) rise. Subsequent drops in total energy inside the particle when backward or forward jets are formed are too small to show on the plots, and the main indications of jet generation events are the short "jiggles" on the maximum $|E_z|$ curve in 7a, which are observed to occur when counter-propagating packets coalesce. This comment on event timing will be made clearer below. The dotted curve in panel 7f is a copy of the internal energy curve shown in Fig. 7b, and is included as an aid in recognizing the phasing of internal and external events. The amplitude scale in panels 7a, 7b, 7e, and 7f is logarithmic; the subsequent pulse emissions are not nearly as clearly defined as the first in the total energy fields in this circular case, but they can be recognized by the episodic burst-like behavior of the interior grid point maximum $|E_z|$.

The two bottom panels in each column show the positions of grid point $|E_z|$ maxima, recorded in (r, θ) form. Recall from Fig. 4 that $\theta == 180$ corresponds to the entry point of the pulse, the direct back-scatter angle, and $\theta = 0$ corresponds to the forward-scatter angle. Thus the "bottom" edge of a θ plot in the panels corresponds to the "bottom" of the circular boundary in Fig. 5(a–l). In Fig. (7c and g), which show radial position, a solid red line has been added to indicate the distance corresponding to the radius of the particle. There are some numerical difficulties in tracking locations of maximum $|E_z|$ when, as appears to be the case in the panels of Fig. 5, that maximum is attained along a curve rather than at a single point, in a locally ripple-like structure. Adding to the difficulty of interpreting movement of maxima is evidence from studies using other methods that there is a very intricate internal field structure near the boundaries [19]. For these and perhaps other reasons the "curves" shown have irregularities that we have not tried to smooth out. In spite of the irregularities certain features are clearly apparent, especially after the main pulse has passed by.

The confinement of maximum interior $|E_z|$ near the boundary of the particle is clear, although there is some indication of a "hopping" between two preferred near-boundary positions that eventually disappears. This hopping may be an artifact of the algorithm used to find the maximum, but it also may be related to the complicated near-surface structure reported in [13], a structure that our numerical resolution perhaps only poorly represents. The θ_{max} plots in panels 7d and 7h show that, after the incident pulse has passed by, the movement of maximal $|E_z|$ location around the particle boundary, described qualitatively above in connection with Fig. 6, does appear to be at a constant angular velocity. More will be said about this movement below.

The θ_{max} plots help "time" events in the other panels of Fig. 7. The three short bursts of interior $|E_z|$ maximum of similar shape seen in Fig. 7a mentioned above are clearly associated with the interaction of the counter-rotating wave structures mentioned above that leads to the emission of pulses. The times at which the locations of maximal $|E_z|$ outside the particle are far away from the particle primarily occur in the period between the first forward "nanojet" pulse (Fig. 5d) and the first backward pulse (Fig. 5h). The first two outward movement events are related to parts of the incident pulse that passes by the particle (before the wide dip of the θ_{max} curve near $\theta = 0$) and the nanojet pulse itself (during the wide dip). The third outward movement of the exterior field maximum occurs before the first backscatter pulse, between the times of panels 5f and 5g. It is part of a broad outward-sweeping field structure that trails back from the departing nanojet pulse, maintaining a weak but clear connection to the field inside the particle as it spreads away from it until it is absorbed by the UPML. Fig. 5m, showing the E_z field at a time intermediate between that of Fig. 5f and g, shows some of this structure. The last two evident outward $|E_z|$ movements correspond, as Fig. 7h shows, to the first back-scatter pulse and the second forward-scatter pulses.

Returning to the observation that the internal field $|E_z|$ maximum appears to travel at an approximately constant angular velocity once the main part of the incident pulse has passed by, the approximate constancy suggests a consideration of how the related speed might compare with the speeds corresponding to the indices of refraction of the particle and of the surrounding medium. An attempt to measure the implied speed of movement, using radial position and a finite difference approximation for angular velocity, was only partly successful, partly because of the "hopping" of radial position mentioned above and partly because of the difficulty of numerically differentiating a noisy θ time series. Fig. 8 shows the result. In the figure the approximately measured tangential speeds are scaled by the speed of light c outside the particle. The three horizontal lines in the tangential speed plot correspond to the outside speed (uppermost line), the speed in the particle (lowest line, at ordinate 1/m), and the average of the two. Given all the uncertainties of the measurement, it is hard to conclude more than that the speed of travel is almost always less than c and is most of the time greater than the speed in a homogeneous medium with index of refraction m.

It is much easier to track amplitude maxima and energy ejection events than it is to characterize the intricate internal structure, structure that connects localized near-surface "wave-packet-like amplitude maxima on opposite sides of the particle. Before turning to consideration of how packet-like behavior and internal wave structure evolves in other particles, we first recall in the next section an idealized model that illustrates in a simple way traveling wave speed determination and connection of near-surface maxima on opposite sides of a particle through internal structure.

3. Phase speed and structure in a "slab" model of traveling waves

The 2-d Maxwell Eqs. (1.1) in the case (1.2) that we have been considering yield a wave equation for the electric field component E_z:

$$\frac{\partial^2 E_z}{\partial t^2} = \frac{c^2}{\epsilon}\left(\frac{\partial^2 E_z}{\partial x^2} + \frac{\partial^2 E_z}{\partial y^2}\right) \tag{3.1}$$

The previous section, as well as the sections to follow, considered properties of numerical solutions to this equation in the case of a 2-valued permittivity. The index of refraction $m = \sqrt{\varepsilon}$, has been assumed to have just two values: 1 outside the particle and some real number greater than 1 within the particle. The problem is a

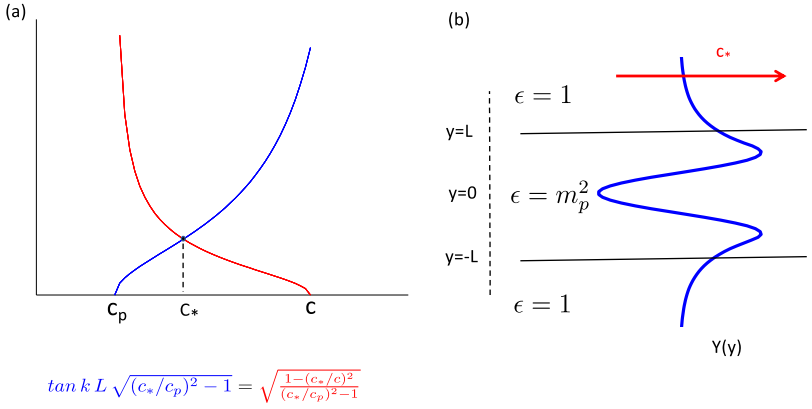

Fig. 9. (a) Graphical demonstration of the existence of a solution to the transcendental Eq. (3.10) and (b) geometry of slab model and structure of gravest even mode.

classical one, and separable solutions for some simple geometries have been thoroughly studied.

The particularly simple model we consider is one consisting of a uniform dielectric slab in a background dielectric medium: in our case the background medium is a vacuum. We recall here elements of the argument for traveling waves in that model: details may be found in [20,21]. The "particle" is an infinite strip of width 2 L oriented along the x axis. The spatial dependence of the index of refraction is assumed to be

$$m(y) = \begin{cases} 1 & y > L \\ m_p & -L \le y \le L \\ 1 & y < -L \end{cases} \tag{3.2}$$

(See Fig. 9b.) With c_* denoting the wave speed, we look for solutions of the form

$$E_z(x, y, t) = \cos(kX)Y(y), \;\; X = x - c_* t \tag{3.3}$$

These are waves traveling in the x direction with a speed c_* that is not a priori known: its determination is made by boundary conditions at the particle boundary and depends on m_p, k, and L in addition to those conditions. Substitution of this form in the Eq. (3.1) results in the relation

$$Y'' - G(y)Y = 0 \tag{3.4}$$

where the y-dependent expression G(y) is

$$G(y) = k^2 1 - \frac{c_*^2 m^2}{c^2} \tag{3.5}$$

The function G(y) is piecewise constant, with jumps at y = L and y=−L; in the context of quantum mechanics, G is a "square well potential." The natural choice for a solution Y(y) is one that is continuously differentiable everywhere, with a second derivative that has a jump where G does. Away from those jumps, the solution either is oscillatory or exponential in y, depending on the sign of G(y). Motivated by our simulations, we require that Y decay exponentially away from the particle and be oscillatory within the particle. Thus we look for a solution that has a wave speed c_* such that

$$G(y) = \begin{cases} > 0, & |y| > L \\ < 0, & |y| < L \end{cases} \tag{3.6}$$

The fraction appearing in Eq. (3.5) is just the square of ratio of the unknown wave speed c_* to the speed $c_p = c/m$ of an infinite plane wave in a medium with index m_p. So we see that the requirement we place in Eq. (3.8) implies (on the standing assumption that $m_p > 1$), that

$$c_p < c_* < c \tag{3.7}$$

i.e., that the unknown wave speed is intermediate between the speed within and without the particle.

This result, which was seen in the numerical experiments, here is a direct consequence of the wave equation and the assumed qualitative structure in y of the solution. The next step in the argument is to find a value of c_* that allows satisfaction of the conditions of continuity of Y(y) and Y'(y) at the boundaries of the particle. Making use of the observation that because the second derivative operator is even, and the geometry of the problem is by construction even in y, solutions exist which are either even or odd in y. The even solution most suits our purpose; the odd solution is no different as far as our main points are concerned. With the definitions

$$l_0 = \sqrt{G} = k\sqrt{1 - \left(\frac{c_*}{c}\right)^2}, \;\; |y| \ge L$$

$$l_1 = \sqrt{-G} = k\sqrt{\left(\frac{c_*}{c_p}\right)^2 - 1}, \;\; |y| \ge L \tag{3.8}$$

the even solution may be sought in the form

$$Y(y) = \begin{cases} Y_0(y) = Ae^{-l_0(y-L)} & y \ge L \\ Y_1(y) = B\cos(l_1 y) & -L \le y \le L \\ Y_2(y) = Ae^{-l_0(-L-y)} & y \le -L \end{cases} \tag{3.9}$$

Requirement that Y and Y' are each continuous at y=L and Y=−L then lead in the usual way to a relation that can be written in the form

$$\tan\left[kL\sqrt{(c_*/c_p)^2 - 1}\right] = \sqrt{\frac{1-(c_*/c)^2}{(c_*/c_p)^2 - 1}} \tag{3.10}$$

The unknown in this equation is the traveling wave speed c_*. The easy way to see that a solution must exist is the graphical method, namely by consideration of what graphs of the right- and left-hand sides of Eq. (3.10) must look like as functions of c_* in the interval between c_p and c. Solutions to Eq. (3.10) occur when those curves intersect and a simple argument shows that there must be (at least) one intersection.

As c_* decreases toward c_p, the right-hand term grows without bound, while, as c_* increases toward c, that term goes to zero. Hence the right-hand term can have all positive values, and a graph of it would be a curve monotonically falling to zero as c_* increases from c_p to c. The exact form of this curve is shown in red in Fig. 9a. On the other hand, the left-hand term is zero at $c_* = c_p$, and initially rises with the increase of argument for the tangent function. The upper limit of that argument occurs when c_*=c, in which case the term on the left-hand side of Eq. (3.10) becomes

$$\tan\left[kL\sqrt{(c/c_p)^2 - 1}\right] = \tan\left(kL\sqrt{m^2 - 1}\right) \tag{3.11}$$

Since the graph of the right-hand term of Eq. (3.10) is a monotonically falling curve covering all positive values, an intersection must occur if the product kL is large enough: with L fixed, this means if the wavenumber k is large enough. The blue curve in Fig. 9a is a graph of the left-hand side of Eq. (3.10), drawn in the case that kL is large enough that an intersection can occur. (As kL continues to increase, more solutions are possible [20,21], but our purposes are served by considering just the first solution that emerges.)

Fig. 9b shows qualitatively the structure of Y(y) that corresponds to the indicated intersection. It is immediately clear why the combined requirements of exponential decay outside the particle, oscillatory behavior inside, and continuity of Y and its derivative lead to a maximum amplitude near but inside the boundary of the particle.

The important features that this simple model demonstrate are that traveling wave solutions have speeds intermediate between the speeds that would be predicted by the indices of refraction of the two media, and that travelling waves with maximum amplitude near the surface have deep "roots" in the interior of the particle, roots that extend all the way through the particle, and in fact connect to the other side. These features are also known to be properties of azimuthally-traveling waves in a circular 2-d particle, the geometry we have considered for the computations in the previous section. The demonstration is considerably more complicated, involving transcendental relations containing logarithmic derivatives of Bessel functions instead of the relatively simple expressions in Eq. (3.10), but the central arguments and results, including a multiplicity of possible modes, are the same. Evidently, the curvilinear beams of large amplitude seen in the Fig. 5(a–l) are due to time-evolving linear combinations of those modes, modes that extend throughout the circular particle. Analogous features will be seen in the results shown in the next section.

4. Pulses generated by curvature maxima

We now consider two cylindrical particles with cross-sections having less symmetry than a circle: an ellipse and a hexagon. These shapes, especially the hexagon, have some relevance to ice crystal scattering studies, but here we just treat them as illustrative of another feature that can excite pulse generation, namely surface curvature variations. We first consider the case of an ellipse oriented with its major axis orthogonal to the direction of propagation of the same incident Gaussian pulse considered in Section 2.

Fig. 10(a–l) show images from a case in which the ratio of the semi-minor axis to the semi-major axis, which we call the aspect ratio, is 0.5, and the size parameter is again $x = 30$. Aside from the fact that Poynting vectors are not shown, the evolution in Fig. 10(a–d) is qualitatively similar to that seen in Fig. 5(a–d) for the circular case. However, the claimed resemblance to "nanojet" formation in the circular case (5d) is less evident in Fig. 10(d), and what appears instead is broader and less focused departing wave. (Anticipating what is seen later in the evolution, we attribute this to a much weaker curvature in the neighborhood of the forward-scattering angle.). Fig. 10(e–g) show something not seen in the circular case: as the wave packets that appear near the surface of the particle pass through $\theta = 90°$ on their trip toward the back-scattering angles, a wave is generated that spins outward, carrying electromagnetic energy away from the particle.

Fig. 10(i and j) shows behavior qualitatively similar to that seen for the circle (5 g,h), but the back-scattered pulse is again broader and less focused in the elliptical case. The remaining panels, 10(k,l) show the same kind of energy release as the near-surface wave packets once again encounter a region of high curvature.

These qualitative statements about the relation between curvature and energy release can be quantified as shown in Figs. 11 and 12. Fig. 11 shows time series of local $|E_z|$ maximum values, total electromagnetic energy, and the (r, θ) position of the $|E_z|$ maximum, inside and outside the particle as in Fig. 7. (As in Figs. 7f, in 11f the internal energy curve is included as a dotted curve.) Again using the θ_{max} time series curve to indicate position, we recognize the intermittent "bursts" in the $|E_z|$ series as corresponding to counter-propagating surface maxima coalescing at direct forward and direct back-scattering angles. Unlike the case of circular cross section, though, the major drops in internal electromagnetic energy do not occur during these events, but instead occur half-way in between them, when the $|E_z|$ maxima enter the regions of maximal curvature. Fig. 11f shows clearly that the significant drops in internal energy that occur then are accompanied by temporary rises in the total exterior energy, a feature harder to see in the case of circular cross section (Fig. 7f); in the latter case the forward- and back-scatter energy release events involve relatively smaller fractions of the particle's total internal energy and so, aside from the first major internal energy release, do not stand out so clearly in either internal or external energy time series.

Also unlike the case of the circular cross section, the angular velocity suggested by the θ_{max} time series in Fig. 11d is no longer constant. This velocity decreases as the wave packets encounter the region of higher surface curvature, where major energy release takes place, then speeds up again once that region is passed. Similar behavior can be seen in the movement of total internal energy, as seen in the middle row of panels Fig. 6b that are for this case. More striking is the appearance in the middle row of panels in Fig. 6a of strong energy maxima outside the particle located at about 90°.

Fig. 12 shows the relation between curvature and energy release for ellipses of two different aspect ratios. Green curves on the figures are for analogous quantities from the circular cross-section case considered in Section 2. (What is in fact plotted for the two different ellipse cases is the radius of curvature divided by the incident Gaussian pulse half-width.) It is immediately clear in the case of the ellipse with smaller aspect ratio ($b/a = 0.5$) that the electromagnetic energy drops most dramatically when the packet carrying the $|E_z|$ maximum enters regions of small surface radius of curvature (i.e. large curvature). This is also true in the case of the ellipse with a larger aspect ratio and hence smaller maximum curvature, but the effect is less dramatic and the rate overall loss of energy by the particle is much closer to that of the circle.

Once the complete symmetry of the circle is broken by passing to an elliptical cross section, there immediately enters another consideration, namely the orientation of the major axis with respect to the direction of propagation of the incident pulse. We do not show here the behavior of the internal wave field when the major axis is parallel to the direction of propagation of the incident pulse, because the regions of maximum curvature are then in the exact forward and backward directions, and the only pulses of energy release are of the sort of seen in the case of the circle: major energy release in jet-like features in the direct forward and direct backward directions when counter-propagating packets coalesce. These jets are more focused than in the circular case. When the major axis has an orientation between these two extremes, mixtures of energy release of both sorts occur but we do not display or comment on them here.

Having seen the effect of curvature in the case of elliptical cross-section, with rate of loss of energy increasing with increased values of local curvature change, we may anticipate what will happen in the case of hexagonal cross-section, where the boundary is a mixture of regions of no curvature and "infinite" curvature (locally straight but non-colinear boundaries meeting). Consideration of the previous cases lead us to expect that most energy release

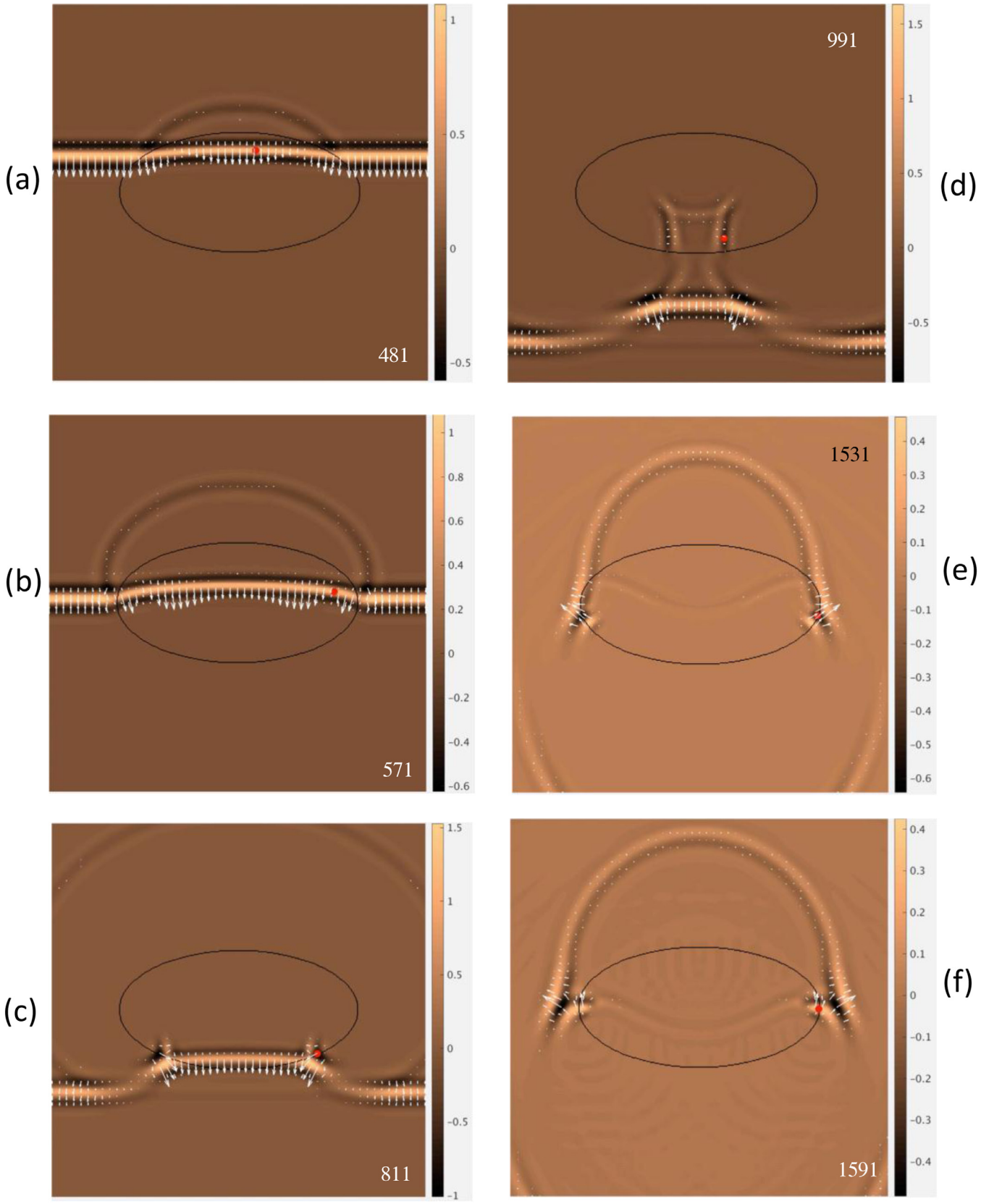

Fig. 10. (a–f). Timesteps 481, 571, 811, 991, 1531, and 1591 in the evolution of the wave field for elliptical cross-section. (g–l). Continuation of previous figure: timesteps 1651, 1801, 1951, 2161, 2551, and 2671.

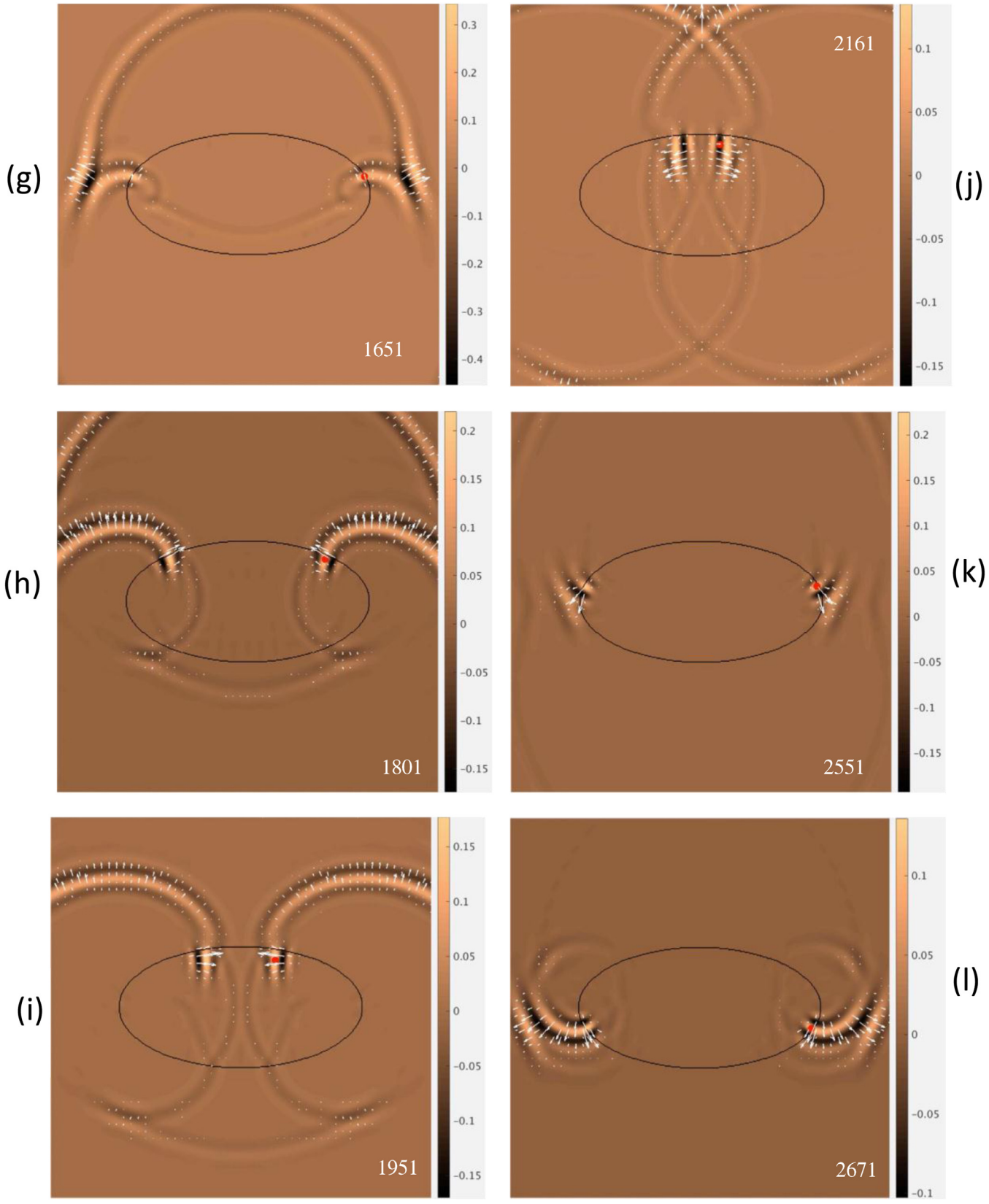

Fig. 10. Continued

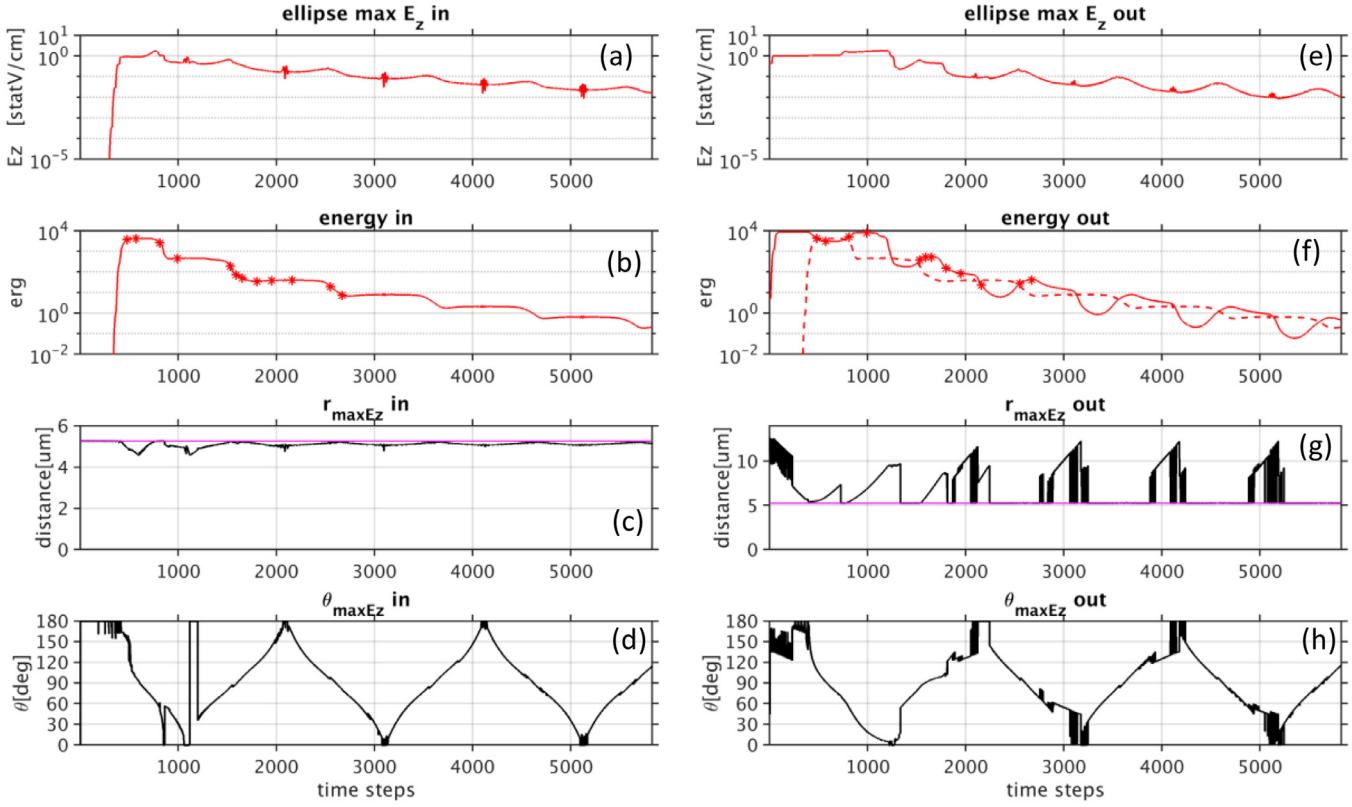

Fig. 11. Elliptical cross section. Time series of $|E_z|$ maximum, total electromagnetic energy, and (r, θ) positions of the maximum, both inside and outside the particle. Asterisks in the second row panels indicate timesteps illustrated in (a–l).

occurs when near-surface amplified traveling wave encounter corners, with relatively little release occurring along straight edges.

Fig. 13 shows selections of images chosen to illustrate typical behavior near corners. The size parameter is the same (30) as in the elliptical and circular cases.

In Fig. 13b, the incident pulse oriented as shown in Fig. 13a has mostly passed out of the computational domain, and the first forward jet pulse has almost exited the region. The red dot in that image indicates a maximum at a midpoint position along the bottom edge of the particle, but evidence can be seen of a leading pair of oppositely propagating features near the boundary. In the next image of the sequence (13c), the internal maxima have moved around the first corner on their travel back toward the back-scatter direction. Note the flux of energy indicated by the Poynting vector that is heading away from the particle parallel to the bottom surface of the particle. Energy shed in this manner, namely parallel to the particle side along which the maximum is travelling when it encounters a corner turns out to be characteristic in the evolution. Fig. 13f and g show this behavior at the next corner, and similar behavior at the top corners (13h) has the effect of actually enhancing the back-scatter jet shown in Fig. 13i. The formation of this jet occurs in a complicated constructive interference between the outward moving wave structure just mentioned generated at each of the top corners by the counter-propagating packets and another generated by the counter-propagating packets when they meet at midpoint along the top edge. The remaining three images in Fig. 13 are for subsequent corner encounters, with the final of the three again showing emergence of a flux that will contribute to another forward-scattering pulse a few timesteps later as described in the back-scattering event of Fig. 13i.

We remark in passing that while images are not shown here that make the point most dramatically, maximum $|E_z|$ often occurs well within the particle, typically along the vertical symmetry axis. Suggestions of how this may occur are seen in Fig. 13(c–e). The occurrence of internal energy maxima at times well within the particle is a common feature of non-circular particles we have investigated.

As was the case for the elliptical particle, the angle-time dependence of the energy outside the particle shown in Fig. 6a (third row) is distinctive. Bursts are recorded at angles near 30° 60° and 120°. The first panel shows in addition amplitude maxima near 180°. Fig. 13i shows the field at a timestep 2281, during the period when the maxima appear: the maxima are clearly a signal of the first back-scattering pulse. The subsequent forward-scattering pulse shows up as the maximum in the lower-right edge of the middle panel at timestep 3500.

Fig. 14, constructed as in Figs. 7 (circle) and 12 (ellipse), shows more quantitatively the major events just described qualitatively. One perhaps surprising finding is the apparent constancy of angular velocity shown in the θ_{max} time series, a constancy not shown in the case of the ellipse. While there is evidence of corner encounters in the movement of the radial position of the $|E_z|$ maxima, there is virtually no impact on the rate of progression of the maxima around the particle. Again, this series serves to indicate the timing of key events: the quasi-periodic bursts of maximal $|E_z|$ in the forward- and back-scatter pulse generation events, the three major drops in internal electromagnetic energy, evidently equally spaced in time between these events that correspond to corner encounters, and near-surface location of the maximal $|E_z|$ at the onset of these energy drops. (Note: the two red lines in the time series for distance from the particle center correspond to the maximum and minimum distances of points on the hexagon from its center.)

Fig. 15 shows time series for the three non-circular cases (two ellipses and one hexagon) and the circular case, green curve. The figure makes it clear that the strong “flattening” of the ellipse with aspect ratio 0.5 has accelerated the rate of release dramatically in comparison with the other cases. While a finding that the

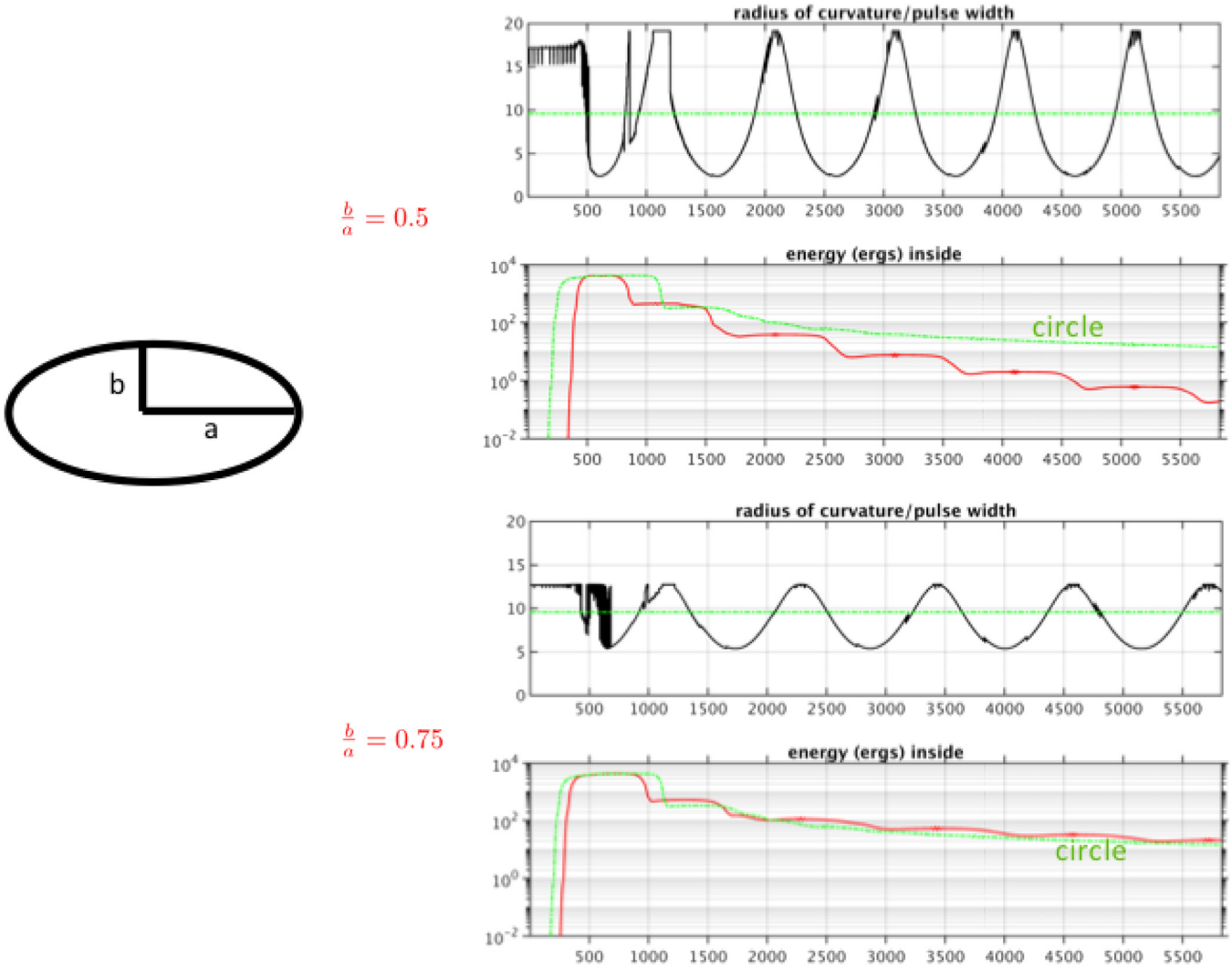

Fig. 12. Time series: surface curvature at point on surface of particle with same angle as nearby interior $|E_z|$ maximum, and total electromagnetic energy, for two aspect ratios. Size parameter $x = 30$ in each case. The energy time series for a circular cross-section particle with the same size parameter is included for comparison.

ellipse with the larger aspect ratio has a rate of energy release closer to that of the circle might be expected, on a view of the ellipse with larger aspect ratio as a less deformed circle, we have no explanation for the fact that the rate of release is actually slower than that of the circle for most of the evolution after the main incident pulse has passed by. This fact stands in the way of making an argument that the faster release of energy from the flatter ellipse might also due to the smaller area enclosed, or the greater ease with which packets can "reach across" the particle when they are traveling on the flattened sides: such arguments would predict the rate of release of the 0.75 aspect ratio ellipse to be greater than, not less than, that of the circle.

We also have no explanation for the fact that the rate of release of energy from the hexagonal particle is similar to that seen in the circular case for a while, but then increases significantly.

5. Summary and concluding remarks

This study was undertaken with the intent of explaining how the intermittent, quasi-periodic oscillatory bursts of electromagnetic field strength at points outside a particle, observed by the authors in previous three-dimensional scattering calculations, might arise. An answer in the case of a one-dimensional scattering model was simple in terms of elementary reflection and refraction arguments, and the next step was to consider two-dimensional scattering.

Using a two-dimensional version of our three-dimensional pseudo-spectral time-domain code, we simulated interactions of Gaussian pulses with particles of circular, elliptical, and hexagonal shape and found in each case that electromagnetic energy trapped after the main pulse passage had an intricate but (in these simple geometries) highly organized form. Although interior maxima of field amplitude were seen at times to appear deep within the particle, for much of the time the field showed maximum amplitude in near-surface wave-packet-like structures that travel around the boundary of the particles when they are "undisturbed." The two kinds of "disturbance" we observed were coalescence with a counter propagating packet, and travel into a region of increased surface curvature. In each case the result was a brief but relatively intense release of energy to the surroundings: given the symmetries of our simple shapes there were always ejections in the direct forward-scattering and back-scattering directions, but changes in curvature led to ejections in other directions. We were able to document the correspondence between energy release and surface curvature, and we pointed out aspects of the evolution that resulted in the generation of two-dimensional "photonic nanojets."

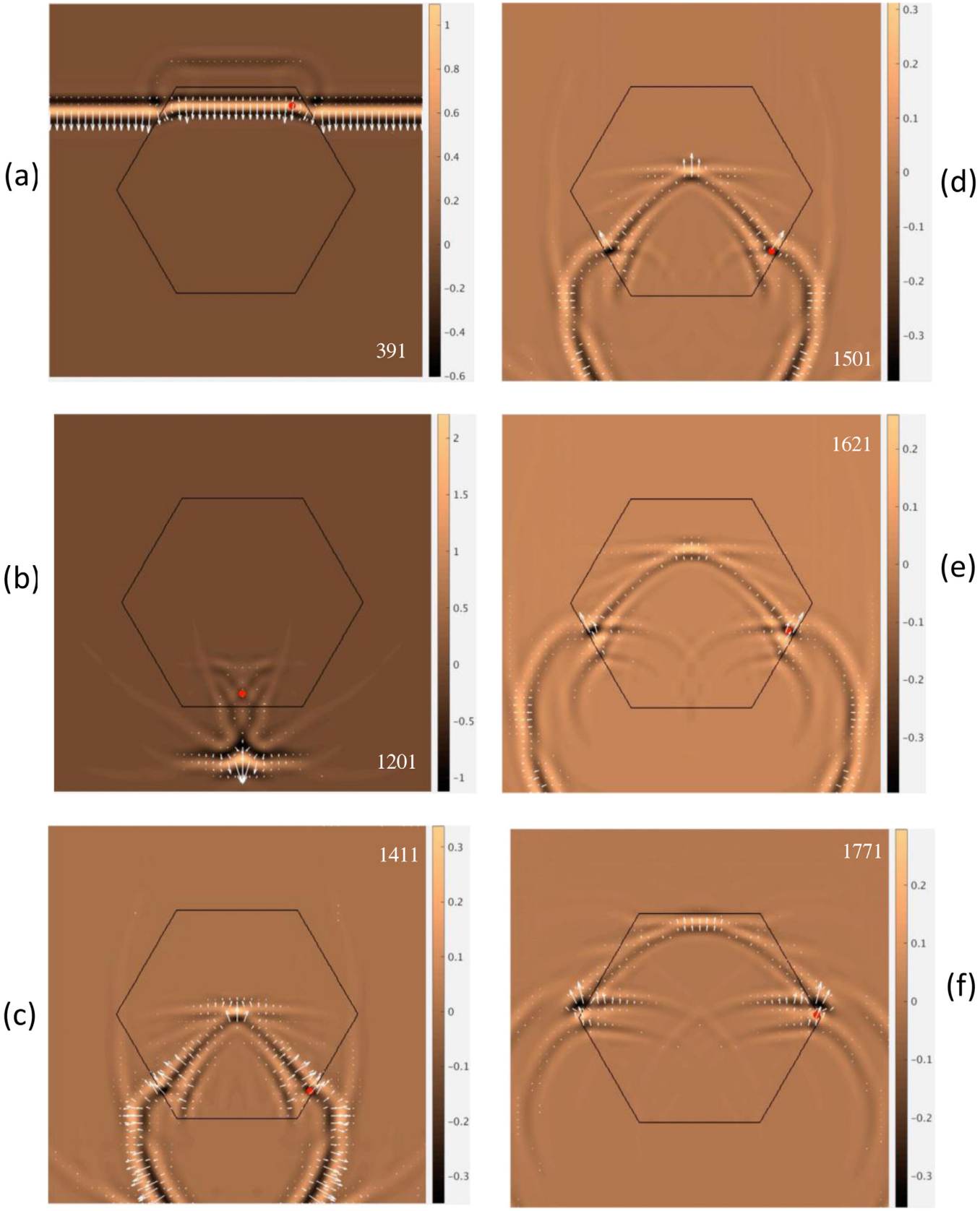

Fig. 13. (a–f) Timesteps 391, 1201, 1411, 1501, 1621, and 1771 in the evolution of the wave field for hexagal cross-section. (g–l) Continuation of previous figure: timesteps 1891, 2131, 2281, 2581, 2911, and 3301. Same size parameter (30) as in elliptical and circular cases.

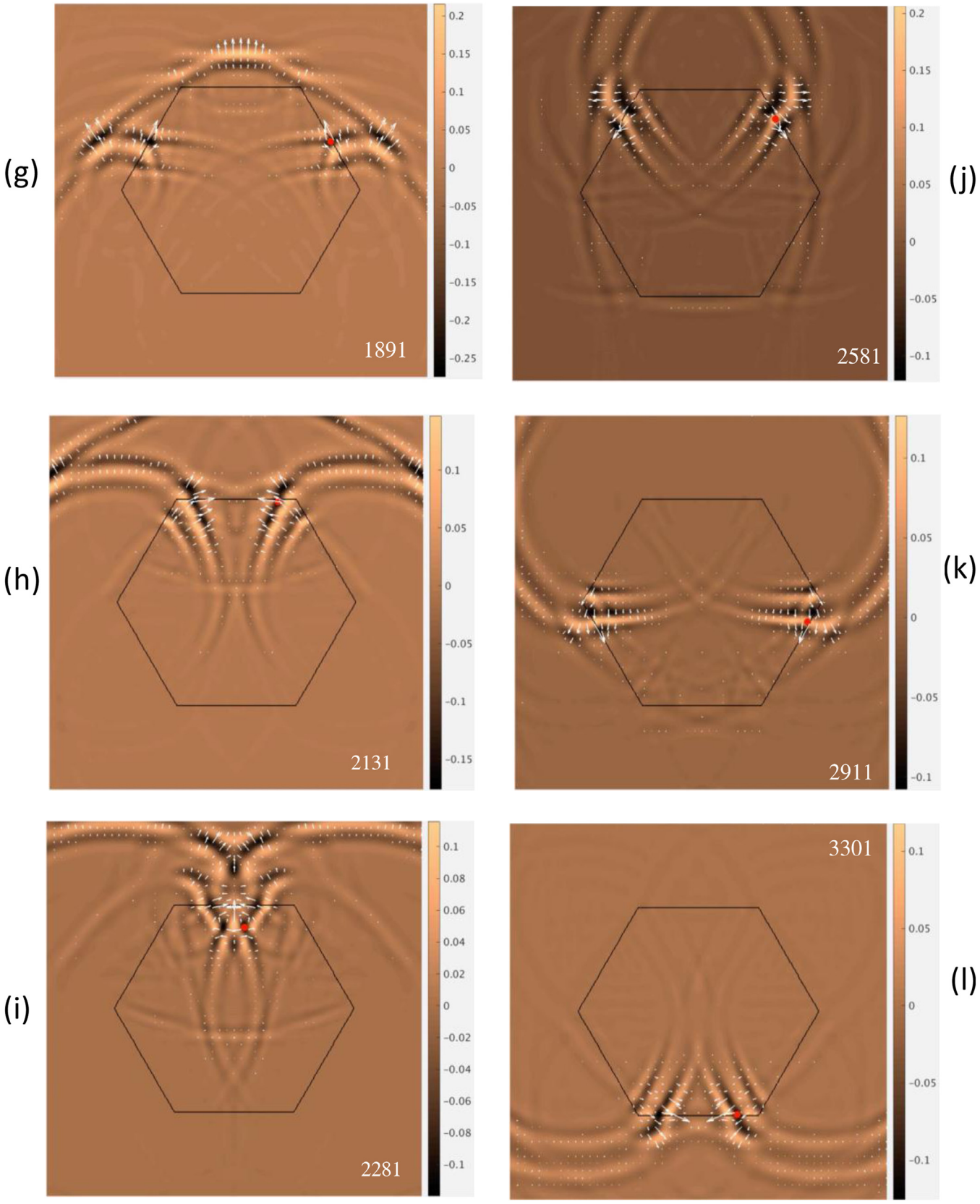

Fig. 13. Continued

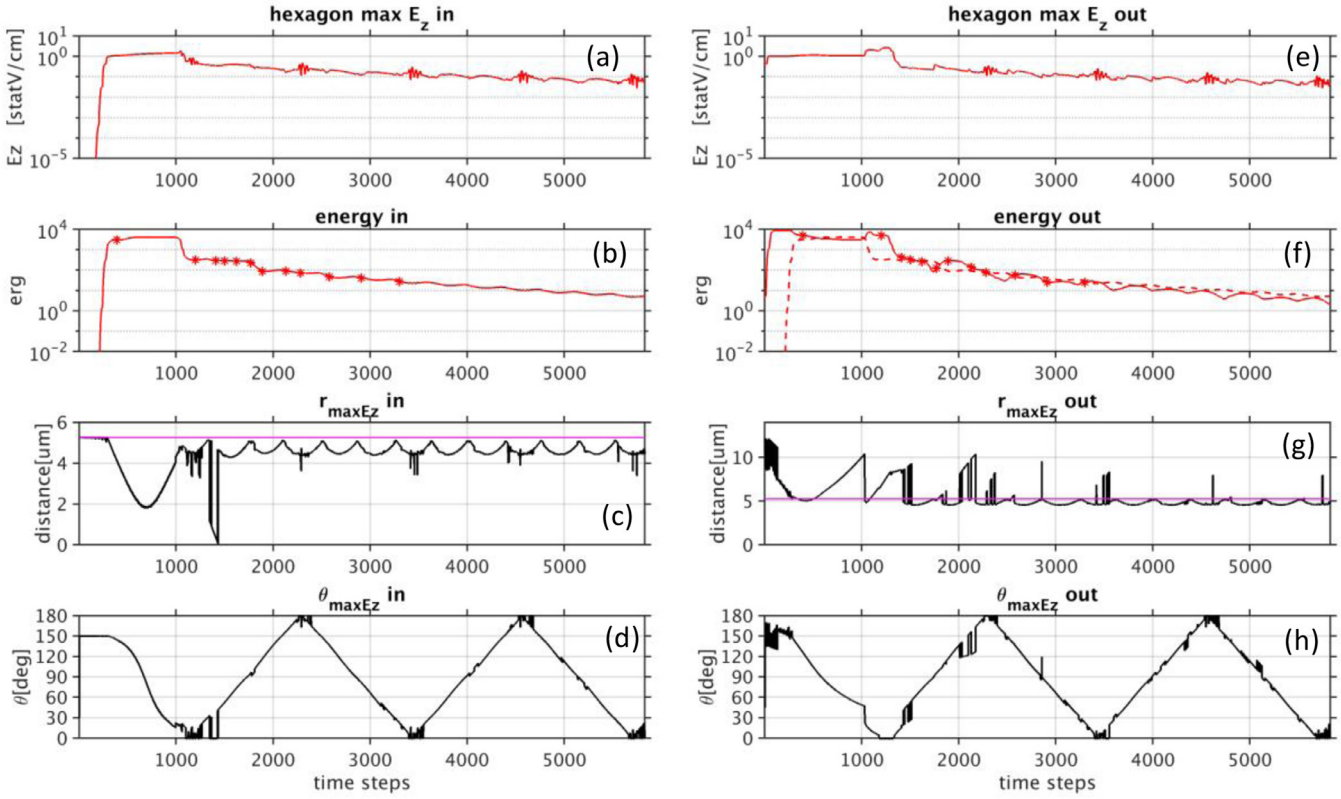

Fig. 14. Hexagonal cross section. Time series of $|E_z|$ maximum, total electromagnetic energy, and (r, θ) positions of the maximum, inside the particle. Asterisks in the second row panels correspond to the timesteps of a–h.

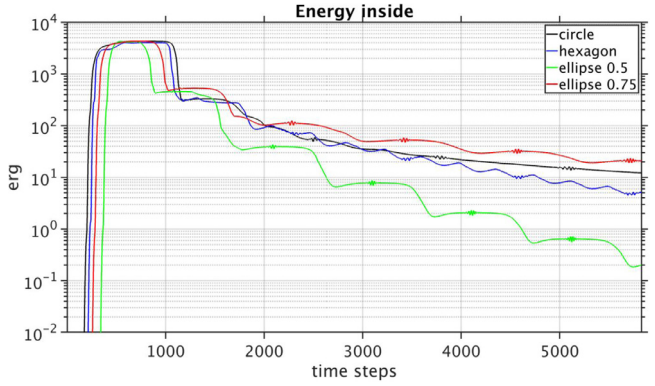

Fig. 15. Comparison of time series of total internal electromagnetic energy for cases of circle (black), the two different ellipses (green for aspect ratio 0.5, red for 0.75), and hexagon (blue). (For interpretation of the references to color in this figure legend, the reader is referred to the web version of this article.).

In spite of the noisiness of the estimate, we were able to show in the case of a particle with circular boundary that near-surface maxima of the electric field travelled at a speed somewhere between the speed intrinsic to the particle and that intrinsic to the surrounding medium, a result familiar from analyses of intrinsic modes in simple idealized models. The regularity observed in the travel speed, combined with the symmetries of the particles considered, and with the oscillatory structure of the outgoing curvilinear "beams," made clear how the electric field behavior at a fixed point outside the particle would show quasi-periodic intermittent bursts of oscillatory field strength.

Even in the context of 2-d simulations with idealized and symmetric particles, there are many ways in which the simple study we have presented might be extended. While a qualitative similarity was observed between the structure of what we called wave packets and the structure of the incident pulse, we have not yet considered just how the structure of the packets is determined by the structure of the incident pulse, nor how the structure of the packet in turn affects the structure of the outgoing energy releases. Details surely involve the geometry of the particle itself. Similarly, effects of incident pulse shape on structure of internal fields and rates of energy release have not yet been investigated, although we have mentioned that changes in the Gaussian half-width parameter σ did affect the amount of energy lost in the pulses emitted in regions of high curvature, particularly in elliptical particle cases.

As far as the structure of the incident pulse is concerned, a more fundamental issue needs exploration: the simulations were conducted using PSTD code that effectively assumes a constant index of refraction for all wavelengths. The calculations are hence "non-diffusive," and while diffusive effects were shown in [12c] to be modest, our finding of sensitivity in energy release to change of incident Gaussian pulse width, which of course means change in the structure of the component frequency band, suggests that non-diffusive effects may also be important. In another vein of exploration, some of the intricacies of the internal field structure field might profitably be explored by considering a time-domain version of the analysis of caustics following the work of [22].

However simple our cases have been, one important feature has been brought out that deserves emphasis. Taken literally, speaking of near-surface concentrations of energy as central features involves taking what is definitely a first-order and highly approximated view. Our simulations show that the surface maxima generally have deep roots within the particle, stretching across the particle to another maximum symmetrically located on an opposing side, and at times field maxima actually leave the surface and appear deep inside the particle.

With the intricacy of the internal field patterns that is revealed in these simple two-dimensional simulations, understanding the physical origin of bursts of energy leaving three dimensional particles, even highly symmetrical ones, may present many surprises. Work in this direction is currently in progress.

Acknowledgments

This study was partly supported by the National Science Foundation (AGS-1826936).

We gratefully acknowledge the computational support of the Texas A&M High Performance Computing Center. We also gratefully acknowledge comments made by J. A. Lock that clarified our thinking on some important points. RLP would like to acknowledge the hospitality of the National Center for Atmospheric Research where he was a visitor while preparing this manuscript.

References

[1] Yee KS. Numerical solution of initial boundary value problems involving Maxwell's equations in isotropic media. IEEE Trans Antennas Propag 1966;14:302–7.
[2] Yang, Liou. Finite-difference time domain method for light scattering by small ice crystals in three-dimensional space. J Opt Soc Am A 1996;13:2072–85.
[3] Liu QH. The PSTD algorithm: a time-domain method requiring only two cells per wavelength. Microwave Opt Tech Lett 1998;15:158–65.
[4] Yang B, Gottlieb D, Hesthaven JS. Spectral simulation of electromagnetic wave scattering. J Comput Phys 1997;134:216–30.
[5] Purcell EM, Pennypacker CR. Scattering and absorption of light by non- spherical dielectric grains. Astrophys J 1973;186:705–14.
[6] Draine BT, Flatau PJ. Discrete-dipole approximation for scattering calcu- lations. J Opt Soc Am A 1994;11:1491–9.
[7] Yurkin MA, Hoekstra AG. The discrete dipole approximation: an overview and recent developments. J Quant Spectrosc Radiat Transfer 2007;106:558–89.
[8] Waterman PC. Matrix formulation of electromagnetic scattering. Proc IEEE 1965;53:805–12.
[9] Waterman PC. Symmetry, unitarity, and geometry in electromagnetic scattering. Phys Rev D 1971;3:825–39.
[10] Mishchenko MI, Travis LD, Mackowski DW. T-matrix computations of light scattering by nonspherical particles: a review. J Quant Spectrosc Radiat Transfer 1996;55:535–75.
[11] Panetta RL, Liu C, Yang P. A pseudo-spectral time domain method for light scattering computation. In: Kokhanovsky AA, editor. Light scattering reviews 8. Springer; 2016. p. 139–88.
[12] Barton JP, Alexander DR, Schaub SA. Internal and near-surface electromagnetic fields for a spherical particle irradiated by a focused laser beam,. J Appl Phys 1988;64:1632–9.
[13] Khaled EEM, Hill SC, Barber PW. Scattered and internal intensity of a sphere illuminated with a Gaussian beam. IEEE Trans Ant Prop 1993;41:295–303.
[14] Laven P. Time domain analysis of scattering by a water droplet. Appl Opt 2011;50:F29–38.
[15] Heiftez A, Kong S-C, Sahakian AV, Taflove A, Backman V. Photonic Nanojets. J Comput Theor Nanosci 2009;6(9):1979–92.
[16] Nussenzveig HM. High-frequency scattering by a transparent sphere. I. Direct reflection and transmission. J Math Phys 1969;10:82–124.
[17] Nussenzveig HM. High-frequency scattering by a transparent sphere. II. Theory of the rainbow and the glory. J Math Phys 1969;10:125–76.
[18] Keller JB. A geometric view of diffraction, in Calculus of Variations and its Applications. In: Graves LM, editor. Proceedings of symposia in applied mathematics, 3. Mcgraw-Hill; 1958. p. 27–52.
[19] Zakowics W. Light rays and imaging in wave optics. Phys Rev E 2001;64:06610.
[20] Jackson JD. Classical electrodynamics. Third edition. Wiley; 1999.
[21] Griffiths DJ. Introduction to quantum mechanics. Prentice-Hall; 1995.
[22] Lock JA, Hovenac EA. Internal caustic structure of illuminated liquid drops. J Opt Soc Am A 1991;8:1541–52.